Lightweight Soft Conductive Composites Embedded with Liquid Metal Fiber Networks

*Jiexian Ma, Zihan Liu, Quang-Kha Nguyen, and Pu Zhang**

J. Ma, Z. Liu, Q. Nguyen, P. Zhang
Department of Mechanical Engineering, State University of New York at Binghamton, Binghamton, NY 13902, United States
E-mail: pzhang@binghamton.edu

Keywords: liquid metal, conductive composites, lightweight, fiber networks, stretchable electronics

Liquid metal composites are promising soft conductors for applications in soft electronics, sensors, and soft robotics. Existing liquid metal composites usually have a high volume fraction of liquid metal, which not only increases the density but also the material cost. Future applications in soft electronics and robotics highly demand liquid metal composites with low density and high conductivity for large-scale, low-cost, lightweight, and more sustainable applications. In this work, we synthesized lightweight and highly conductive composites embedded with liquid metal fiber networks. This new paradigm of liquid metal composites consists of an interconnected liquid metal fiber network embedded in a compliant rubber matrix. The liquid metal fiber network serves as an ultra-lightweight conductive pathway for electrons. Experiments indicate that this soft conductive composite also possesses nearly strain-insensitive conductance and superior cyclic stability. Potential applications of the composite films as stretchable interconnects, electrodes, and sensors are demonstrated.

1. Introduction

Soft conductors[1,2] with high stretchability, superb conductivity, and excellent cyclic stability are vital materials for emerging technological areas such as soft electronics and soft robotics. Compared to intrinsically conductive polymers[3,4] including ionic elastomers, soft conductive composites offer an enormous design space, much higher electrical conductivities, and possibly improved mechanical performance. Soft conductive composites usually consist of a compliant elastomer matrix and one or more conductive fillers, e.g., carbon nanomaterials,

silver nanoflakes, liquid metals (LM),[5,6] ionic liquids, etc. At present, the most promising filler material is liquid metal, e.g. EGaIn and Galinstan. On the one hand, LM's fluidity enables supreme stretchability and inherent self-healing of the soft conductive composites compared to rigid fillers[7,8] such as silver- and carbon-based nanofillers. On the other hand, LM's metallicity enables greater electrical conductivity ($\sigma = O(10^6\ \mathrm{S/m})$) than other liquid conductors[9,10] such as ionic liquids and salt solutions ($\sigma = O(1\ \mathrm{S/m})$). Within the past few years, researchers have made significant progress on the synthesis and applications of LM composites.

So far, researchers mainly developed two types of LM composites: particulate composite[11–21] and co-continuous composite.[22–25] Various matrix materials have been adopted such as elastomers, thermoplastic elastomers, hydrogels, etc. Both types of LM composites are relatively easy to synthesize. Specifically, particulate LM composites can be obtained by mixing either bulk LM or LM particles with elastomer compounds together, followed by a curing process. Co-continuous LM composites are usually synthesized by infilling LM into an elastomer foam directly. The electrical conductivity of the LM composites is mainly dominated by the percolation networks. Particulate LM composites are generally non-conductive after synthesis, and sintering is needed to create percolation pathways among particles. Usually, particulate LM composites need a high filling ratio of LM (typically > 40 vol%) to achieve conductivity. In contrast, co-continuous LM composites are intrinsically conductive after synthesis because of the percolation networks. However, the filling ratio of LM in co-continuous composites is also very high (typically > 30 vol%) due to the limitation of the foam templates. The high filling ratio of LM in existing LM composites has inevitably made them heavy and expensive. Hence, developing lightweight LM composites is one critical bottleneck to further expand the applications of LM in emerging technological areas and industry.[26,27]

In this work, we introduce LM fiber composites (LMFC) as a new paradigm of conductive LM composites, which exhibit ultra-lightweight and high conductivity simultaneously. The proposed LMFC consists of a soft matrix (e.g., silicone rubber) and a LM fiber network embedded in it (**Figure 1**a). This new microstructural design is inspired by the fact that a percolated network with a minimal amount of materials must be a fiber network. The interconnected LM fibers will serve as conductive pathways of electrons. In this work, the LM fiber network is composed of LM-SEBS core-sheath microfibers with a diameter of 10-20 μm (Figure 1b,c). Specifically, these microfibers are fabricated by co-axial emulsion electrospinning with a LM core emulsion and a SEBS sheath solution. In this approach, we circumvent the difficulty of electrospinning LM fibers directly due to the surface tension issue.

Upon mechanical sintering, we obtained LMFCs with an electric conductivity of 1.11 S/mm using only 3.82 vol% of LM. Figure 1d compares the electrical conductivity of our LMFCs with that of the particulate and co-continuous LM composites in the literature. Figure 1d shows that LMFCs fill the material void in the low-density domain on the Ashby chart. LMFCs have an ultimately low volume fraction of LM (~10-fold reduction) while possessing comparable electrical conductivity. With such a significantly reduction of LM filling ratio, the composite products will have much lighter weight, drastically reduced price, less energy consumption, and eliminated leakage, ideally for practical applications in soft electronics and robotics. Moreover, LMFCs exhibit high stretchability (800% strain), nearly strain-insensitive conductance, and superior cyclic stability, which will be shown later. In addition, to demonstrate the functionality of LMFCs, we apply it as interconnects in stretchable circuits and as stretchable electrodes in wearable capacitive sensors. The LMFC interconnects show great reliability under different deformation modes. The LMFC electrodes in capacitive sensors can serve in both stretching and compression modes with outstanding compliance and electromechanical responses.

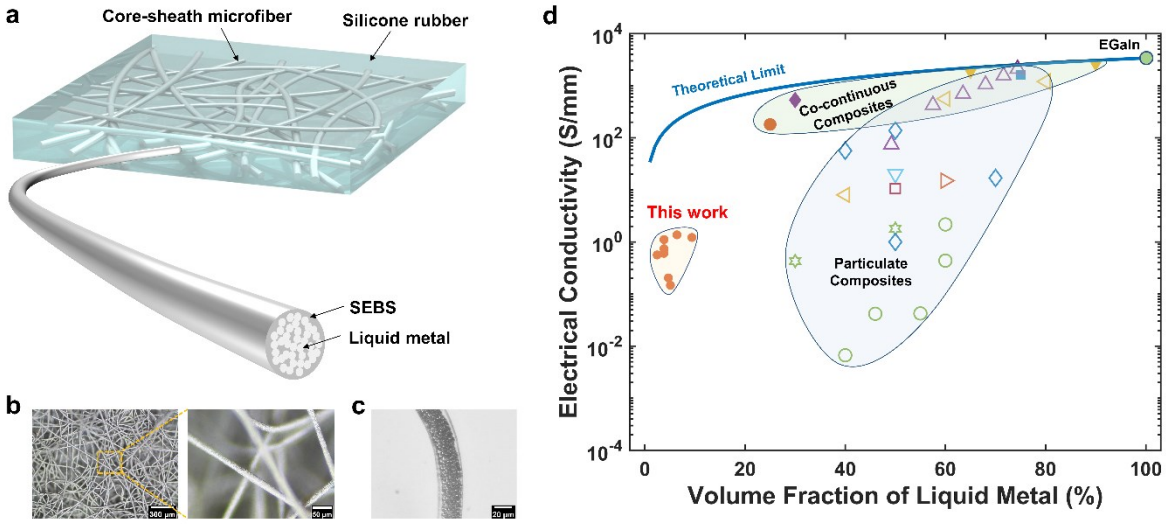

Figure 1. LM fiber network composites (LMFC). a) Schematic illustration of LMFC. This composite consists of an LM-SEBS microfiber mat and a silicone rubber matrix. b) Optical microscope images of a LM fiber mat and c) a single fiber with a LM particle core. d) Ashby chart of electrical conductivity and volume fraction of LM in LM composites in the literature.[11–18,22–26,28] (Detailed data are listed in Table S1, Supporting Information.). The theoretical limit is computed from the rule of mixture: electrical conductivity $\sigma = f\sigma_{LM}$, where f is the volume fraction of liquid metal, σ_{LM} is the electrical conductivity of liquid metal, provided that the matrix is non-conductive.

2. Fabrication of liquid metal microfibers

Very recently, LM fibers have attracted great interests due to their potential applications in E-textile, stretchable circuits, and wearable sensors.[29] Common methods to fabricate LM fibers include coating LM on fibers,[30–34] injection into hollow fibers,[35–38] wet spinning,[39,40] thermal drawing,[41], and electrochemical methods.[42] Among them, coating LM on fibers is the most facile method because it can utilize the existing fabrics or electrospun mat as substrates.[30,33,43] Although the LM coated textiles can exhibit permeability and superelastic behaviors,[31,34] the coating process is difficult to control and the LM coating may degrade in usage. An alternative method is injecting LM into hollow elastomer fibers.[35] With the aid of microfluidic chips, the inner diameter of coaxial LM fibers can achieve 150 μm.[37] Nevertheless, the injection method involves multiple steps and cannot be mass-produced. In contrast, one-step coaxial wet spinning[39,40] or thermal drawing[41] can realize continuous and mass production, but the diameter of obtained fibers is usually thick (>200 μm). One novel strategy to reduce the diameter of wet spun LM fibers is to lower the surface/interfacial tension of LM via electrochemical oxidation.[42,44] By tuning electric potential, this remarkable method can produce continuous LM fibers with 100 μm diameter. To collect these LM fibers, interfacial electrochemical polymerization was used to encapsulate the LM.[45]

Fabrication of LM microfibers below 100 μm remains a technical challenge to date. The large diameters of LM fibers produced by the existing methods limit their applications in E-textiles and soft conductive composites. There is a demanding need to discover methods to fabricate LM fibers with diameters around 10 μm or smaller. One popular method to fabricate microfibers (diameter <50 μm) in large scale is electrospinning, which achieves fiber drawing using electrostatic forces. We have tried a few options to fabricate LM microfibers using electrospinning. (1) *Electrospinning of LM*. It is impractical to electrospin continuous LM fibers directly using one spinet for two reasons. On the one hand, the enormous surface tension (>500 mN/m)[46] of LM prevents the formation of a Taylor cone. On the other hand, the negligible viscosity of LM[47] makes it hard to be drawn continuously and encapsulated. (2) *Coaxial electrospinning*. We tried to overcome these difficulties by electrospinning core-sheath fibers with a LM core and a SEBS sheath. Although the viscosity issue was overcome, it was impossible to form a compound Taylor cone because of the enormous surface/interfacial tension of LM. Only a spherical LM bubble was formed in the Taylor cone (Figure S1a, Supporting Information). (3) *Emulsion electrospinning*. Researchers have fabricated LM composite fibers using emulsion electrospinning with a low volume fraction of LM nanoparticles (0.35-6.5 vol%, details are listed in Table S2, Supporting Information).[48–50] However, none of these fibers are

conductive. We tried to electrospin a LM-SEBS emulsion with LM:SEBS=80:20 by volume. The electrospinning process was partially successful given the formation of a stable Taylor cone. But the emulsion fiber was too fragile to form a continuous fiber, implying the necessity to encapsulate it. (4) *Coaxial emulsion electrospinning*. This method utilizes the LM-SEBS emulsion as the core fluid and a SEBS solution as the sheath fluid. Specifically, the core emulsion overcomes the surface/interfacial tension and viscosity issues of LM; and the SEBS sheath overcomes the fiber strength and encapsulation issues. We were able to produce core-sheath LM-SEBS microfibers around 10 μm successfully. The details will be introduced next.

In this work, we circumvent multiple technical challenges by adopting this coaxial emulsion electrospinning method (Figure 2a) with a LM-SEBS emulsion as the core fluid and a SEBS solution as the sheath fluid. The LM-SEBS emulsion was produced by dispersing EGaIn microdroplets (1-3 μm) in SEBS-chloroform-toluene polymer solution (EGaIn:SEBS = 80:20 by volume). This emulsion has a high dose of LM to improve the electrical conductivity. Meanwhile, SEBS was added to the core emulsion to tune viscosity so that the LM particles do not sediment. Note that the core fluid does not need a high viscosity for electrospinning. Under the shield of the SEBS sheath solution, a stable compound Taylor cone formed at the nozzle tip (Figure S1b, Supporting Information), and continuous LM-SEBS core-sheath microfibers were deposited on the collector. Note that without the sheath solution, the core emulsion is too fragile to form a continuous fiber. As shown in Figure 1c and Figure 2b, the obtained LM-SEBS core-sheath microfibers consist of a LM-rich core and a thin layer of SEBS sheath. The volume loading of LM in the fiber core is about 80 vol%, while the overall volume loading of LM in the mat is 50-60 vol% by including the SEBS sheath. By tuning electrospinning parameters including solution properties, flow rates, and applied voltage, we can collect LM microfiber mats with various fiber diameters and different thickness of SEBS sheath. With the parameters presented in Section 6, we obtained a uniform LM-SEBS fiber mat with an average diameter of 15.93 μm (Figure 2b) and with a sheath thickness of 1-2 μm. Note that existing technologies can only make conductive LM fibers thicker than 100 μm, while this work achieves 10 times thinner at ~10 μm. In theory, this fabrication method can produce even thinner fibers if finer LM nanoparticles are used. However, LM nanocomposites[51] have their own shortcomings such as rigidity, sintering, and percolation issues and will not be explored in this work.

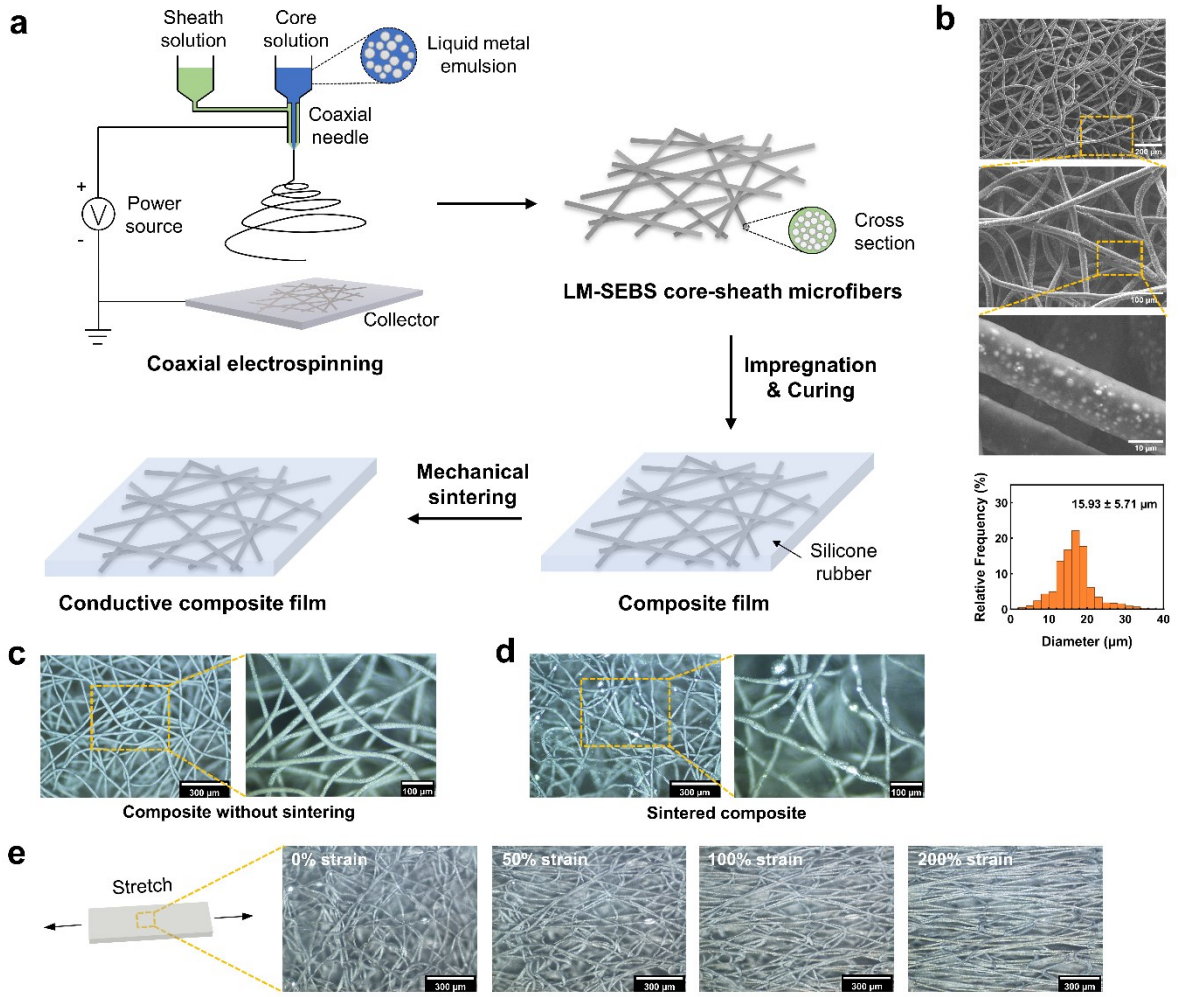

Figure 2. Fabrication methodology and microstructures of the liquid metal fiber composites (LMFC). a) Fabrication procedure of LMFCs. The LM-SEBS microfibers are produced by coaxial emulsion electrospinning with a LM-rich core fluid and a SEBS sheath fluid. A composite film is obtained by impregnation of electrospun LM-SEBS fiber mats with silicone rubber. Mechanical sintering is used to activate the electrical conductivity of the composite film. b) Scanning electron microscopy (SEM) images and diameter distributions of the LM-SEBS microfiber mat. Optical microscopy images of the composites and fibers c) before sintering and d) after sintering. After mechanical sintering, LM leaks out from the fiber core and forms percolation networks within and between fibers. e) Microstructural evolution of the sintered composite under stretching (up to 200% strain level). Fiber alignment and stretching is observed under optical microscopy.

3. Results and Discussion

3.1 Microstructures

The LM-SEBS fiber mat is cut and impregnated with silicone rubber (Ecoflex 00-30) to obtain an LMFC film. Although the core of the microfiber is LM-rich (80 vol%), the obtained LMFC film (~ 0.3 mm thick) is still electrically non-conductive before mechanical sintering, which is attributed to the insulated oxide layer on LM particles and insulated SEBS phase in the fibers.[16] To activate electrical conductivity, local pressure is applied to the surface of the composite film. Under mechanical stress, the oxide layer of LM particles and the SEBS phase between particles rupture, and the LM particles are sintered and percolated together to form conductive pathways.[52] The sintered composite with a gauge length of 10 mm and a width of 3 mm can exhibit resistances of 2-15 Ω. The resistance of the LMFC film is highly dependent on the area density of the embedded fiber mat. In our specimens, the typical area density of LM fiber mat is 0.01-0.02 g/cm^2. Based on the measured resistance and sample size, we calculated the electrical conductivity of LMFCs with different LM volume fractions (Table S3, Supporting Information). One of the best is the composite with a conductivity of 1.11 S/mm when the volume fraction of LM is 3.82% in the LMFC film. Compared to other conductive LM composites, the LM volume fraction of our LMFCs is significantly lower (Figure 1d). We can reduce the LM material consumption to 10% of the current one with comparable electrical conductivity. Moreover, we observed that mechanical sintering at high temperature (>130°C) can further reduce the resistance of the composite (Table S4, Supporting Information). Since SEBS in the core-sheath fiber is softened at high temperature, SEBS surrounding LM droplets can deform easily and facilitate the sintering process. Mechanical stretching can also activate conductivity but a large strain (>500%) is required to observe a substantial resistance drop (Figure S2, Supporting Information). Our discoveries on sintering LMFC are consistent to the findings from the literature for LM particulate composites.[15,16,53]

Comparing the microstructures of the sintered composite with the unsintered one, we observed that LM microdroplets in the fibers were sintered and coalesced into much larger droplets (Figure 2c,d). Some sintered LM droplets were squeezed out of the SEBS sheath of the coaxial fibers, which indicates the SEBS sheath layer is ruptured under the sintering force. The fibers become slightly curvy in sintered composites, which is reasonable since the mechanical sintering process introduces distortion and damage to the microfibers, considering the fact that both SEBS and the surface oxide may contribute to plastic deformation. According to optical microscopy images, some fiber junctions are connected after sintering whereas some do not

change. The electrical conductivity of the LMFC will definitely depend on the connectivity of fiber junctions. In theory, the conductivity is higher if more junctions are connected or welded.

To examine how the microstructure of LMFCs changes under stretching, we mounted a sintered sample to a micro-stretcher and took microscope images at different strain levels (Figure 2e). Curvy fibers are straightened at 50% strain, and fibers become more and more aligned in the stretching direction as the composite is continuously stretched. We do not observe any fractured fibers during stretching. The mechanical deformation of the LM fiber network is almost affine following the global deformation of the whole composite film. Note that the LM fibers cannot withstand much stress, but they can sustain a high strain level like liquids. Once they are embedded in a rubber matrix, they can withstand large deformation without failure.

3.2 Mechanical and Electromechanical Behaviors

We performed uniaxial tensile testing to characterize the mechanical behaviors of LMFCs (Figure 3a). Overall, the LMFC behaves like a hyperelastic rubber material because of the low volume fraction of LM and SEBS in it. With LM-SEBS microfibers embedded, the modulus (defined as the stress at 100% strain here) of the composite significantly increased (83.53 kPa, ~3.2 folds, Figure S3a, Supporting Information) compared to Ecoflex 00-30. This strengthening effect is attributed to the higher modulus of the thermoplastic elastomer SEBS, compared to that of the elastomer Ecoflex 00-30. The surface oxide of the LM droplets may contribute to the stiffening of the LMFC as well but need to be evaluated in the future. The mechanical sintering process does not affect the stiffness of the LMFC samples, although slightly lower stress is observed for the sintered sample at high strain levels. Moreover, the strain at break for LMFC (~ 800%, Figure S3b, Supporting Information) is lower than that of the silicone rubber (~ 1000%) since SEBS has a smaller failure strain (~750%). Compared to pristine silicone rubber, the LM fiber networks play a role of voids or defects in the rubber matrix, which reduce the maximum failure strain.

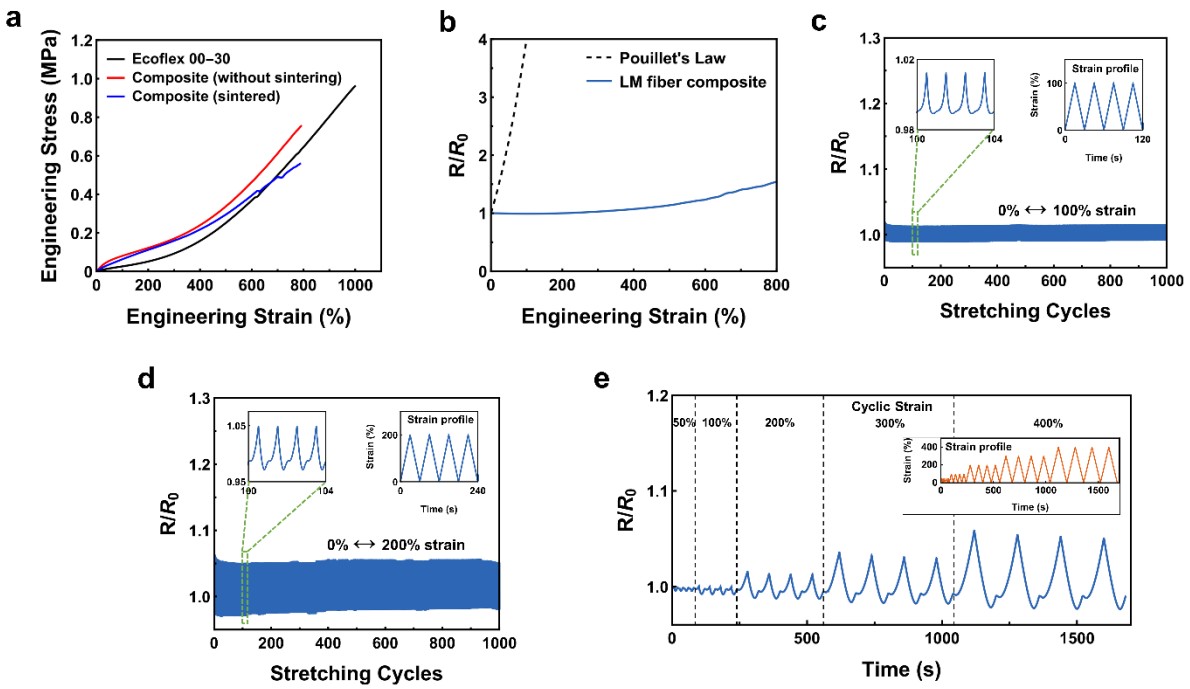

Figure 3. Mechanical and electromechanical behaviors of LMFCs. a) Typical stress-strain curves of LMFC with and without sintering. b) Normalized resistance of LMFCs versus tensile strain. c,d) Normalized resistance of LMFCs during cyclic stretching for 1000 cycles: c) 0-100% strain, and d) 0-200% strain. The left inset shows a zoom-in for the 100-104th cycles. The right inset shows the strain profile. e) Resistance responses of the composite under cyclic stretching with progressively increasing strain levels (50%, 100%, 200%, 300%, and 400%). The inset shows the strain profile.

To characterize the strain-dependent electromechanical behaviors of LMFCs, we monitored the resistance change using a multimeter when stretching the specimen on a tensile tester. As shown in Figure 3b, the resistance of LMFCs remains almost constant when stretched to 400% strain, in contrast to Pouillet's Law. Normalized resistance (R/R_0) of the LMFC is as low as 1.072 at 400% strain and 1.543 at 800% strain. Beyond 800% strain, the resistance drastically increased as the composite reached failure strain. The LMFCs show strain-insensitive resistance under large deformation, which is desirable for the application as stretchable interconnects and electrodes. This remarkable feature of LMFCs is similar to the behavior of LM particulate composites. Note that the LM microfibers are indeed made of LM particulate composites with a high dose of LM in this work. The mechanism of strain-insensitive resistance of LM particulate composites was well explained by Majidi [54,55]. Their research found that the tortuous morphology of conductive pathways between LM droplets is the primary reason for the strain-insensitive resistance for large deformation. This phenomenon

also indicates that although LM particulate fibers have lower conductivity than pristine LM fibers, the strain-insensitive resistance is a remarkable advantage for application purposes.

It is worth noting that the silicone rubber matrix plays a crucial role in our composite. The LM fiber mat is super-stretchable (up to 600% strain) but very fragile, because of the high dose (80 vol%) of LM in the fiber cores. Encapsulation of LM fibers in silicone rubber can effectively address the issues of leakage and damage. For instance, during mechanical sintering of LM-SEBS fibers (without encapsulation), we observed significant leakage of LM from the fibers and even damage of the mat. The silicone rubber encapsulation notably enhances the structural integrity and the electromechanical performance of the LM fibers.

The LMFCs have outstanding electrical stability under cyclic stretching. We recorded resistance changes when LMFCs were subjected to cyclic triangular strain (0-100% or 0-200%) for 1000 cycles, as shown in Figures 3c and 3d. For specimen subjected to 0-100% strain, the computed R/R_0 changed in the range of 0.992 to 1.015 at the end of 1000 cycles. For specimens under 0-200% strain, its R/R_0 varied between 0.981 and 1.05 at the 1000^{th} cycle. Such superior reliability of LMFCs will greatly benefit wearable electronics and soft robotics. To evaluate its electromechanical performance at multiple strain levels, we stretched LMFCs with progressively increasing strain. As shown in Figure 3e, the electrical response of LMFC is highly consistent and repeatable within a specific strain level. Another interesting phenomenon observed from Figure 3c-e is the phase delay of the resistance response compared to the strain loading. This phase delay is attributed to the viscous effect of the LM flow under cyclic loading.

4 Potential Applications

4.1 Interconnects

The LMFCs are ideal soft conductors for interconnect applications in stretchable and wearable electronics because of their lightweight, high conductivity, superb stretchability, and cyclic stability. With the material properties of LMFCs characterized, we now demonstrate that LMFCs can be utilized as interconnects in stretchable circuits. As shown in Figure 4a, an LED is connected to a power source using a thin LMFC strip, and the current of the connected circuit is measured by a multimeter. As the composite film is stretched to ~500% strain, the current changed from 0.717 mA to 0.594 mA, and the LED maintained its initial brightness during stretching (Video S1, Supporting Information). In contrast, when the circuit is connected using a LM-infilled channel (160 μm in diameter, pristine LM) instead of LMFC, we observe a dramatic dimming in the LED as the LM channel stretched to ~250% strain (Figure S4, Supporting Information). The dimming is caused by the dramatic resistance increase of the LM-

filled channel under strain, which follows the Pouillet's law. This example highlights the enormous advantage of LMFCs, i.e. strain-insensitive resistance under large strain, which is favored for stretchable interconnects.

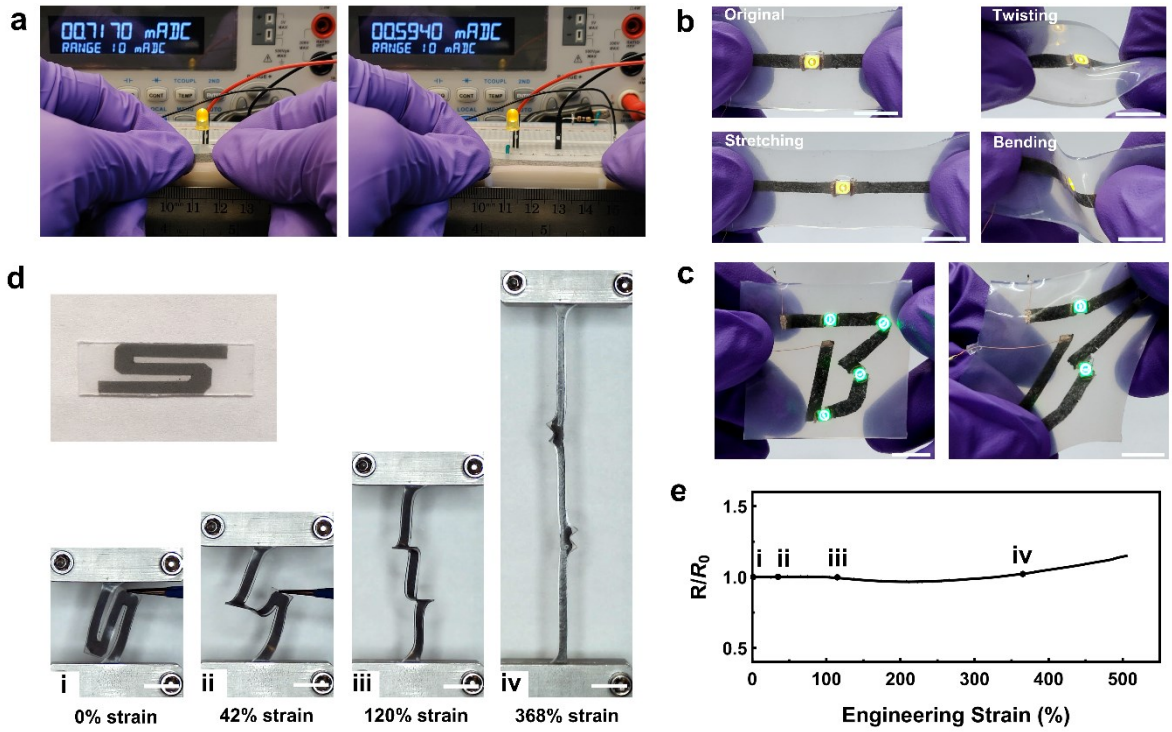

Figure 4. Demonstration of LMFCs as interconnects. a) LED connected to a power source using a LMFC strip. The brightness of the LED does not change when the LMFC is stretched. b) Stretchable circuit integrated with surface mount LED enabled by LMFC. The circuit is reliable under various deformation modes such as stretching, twisting, and bending. Scale bar, 10 mm. c) B-shape circuit with multiple surface mount LEDs. Scale bar, 10 mm. d) Stretching of an S-shape interconnect. Scale bar, 10 mm. e) Normalized resistance as a function of tensile strain for the S-shape interconnect in d). (i-iv) correspond to 0%, 42%, 120%, and 368% strain, respectively. The resistance is almost strain-insensitive.

To demonstrate the compatibility of LMFCs with surface mount rigid electronics, we integrated LMFC with a surface mount LED (Figure 4b; Video S2, Supporting Information). Legs of the LED were bonded to the LM fiber mat using conductive paste. After encapsulating the structure in silicone rubber, mechanical sintering was applied to LMFC to activate conductivity. The obtained circuit can maintain its functionality and integrity under various deformation modes such as stretching, twisting, and bending. Furthermore, we show a B-shape circuit with multiple surface mount LEDs integrated (Figure 4c). The LEDs displayed constant

brightness when the circuit was stretched. However, we note that the stretchability of the above circuits is limited (<200%) due to the stiffness mismatch between LMFCs and rigid electronics. This issue could be circumvented by serpentine LMFC structures. When stretched, the serpentine structures would be the primary source of deformation. Here we fabricated a LMFC with S-shape as an example of serpentine LMFC structures and examined its resistance change under stretching (Figure 4d, e; Video S3, Supporting Information). The S-shape LMFC is highly deformable and exhibits negligible resistance change when stretched to 500% strain.

4.2 Capacitive Sensors

Another promising application of LMFCs is stretchable electrodes since LMFCs have outstanding stretchability and strain-insensitive resistance. We fabricated a capacitive strain sensor with a sandwich structure, which is composed of two layers of LMFC films on the top and bottom and one layer of Ecoflex film in the middle (Figure 5a). This soft strain sensor is able to measure local strain for large deformation. The conductive LMFC films in this device function as stretchable electrodes. Upon stretching, the area of the LMFC electrode is larger and the Ecoflex film in the middle is thinner, which results in capacitance change of this capacitive sensor. To characterize the behavior of the produced strain sensor, we measured capacitance while stretching the sensor on a tensile tester simultaneously. The initial capacitance of the sensor is 2.957 pF. The strain sensor exhibits a large linear region (0-300% strain), and the normalized capacitance (C/C_0) is 2.384 at 300% strain (Figure 5b). Besides, the strain sensor has great stretchability (>430% strain), which is desirable for wearable sensors and soft robotics. To demonstrate the practicality of the capacitive strain sensor, we adhered the strain sensor to the index finger of a nitrile glove. As shown in Figure 5c, the strain sensor can effectively detect the bending angle of the finger. For example, the C/C_0 reaches 2.42 when bending to 92°. We also incorporate the strain sensor into a pneumatic soft actuator (Figure 5d; Video S4, Supporting Information) that is frequently used in soft robotics. Due to the compliance and great stretchability of the strain sensor, the mounted strain sensor can deform conformally with the inflated soft actuator and monitor the local strain history. The response of the strain sensor is stable and repeatable when the soft actuator undergoes actuation cycles of inflation and deflation (Figure 5e).

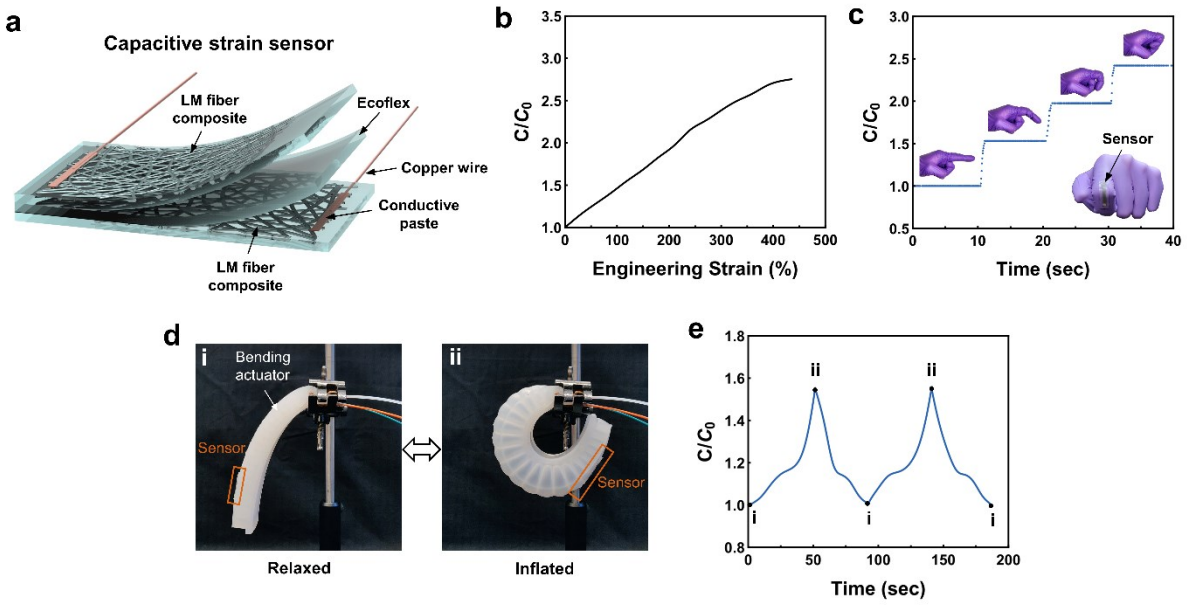

Figure 5. Capacitive strain sensor with LMFC as stretchable electrodes. a) Schematic of the capacitive strain sensor composed of one Ecoflex layer in the middle and two LMFC layers on the top and bottom. b) Normalized capacitance of the sensor as a function of tensile strain. c) Response of the sensor when bending index finger. (The sensor is bonded onto index finger of the glove). d) Photograph of a pneumatic soft actuator mounted with a capacitive strain sensor. One actuation cycle: (i) relaxed, and (ii) inflated. e) Change in normalized capacitance of the sensor during actuation cycles of the pneumatic soft actuator.

The capability of LMFCs as electrodes is further demonstrated in a capacitive pressure sensor. Such kind of sensors are very useful as tactile sensors in wearable electronics and soft robotics. A polyurethane (PU) foam was sandwiched between two LMFC electrodes. To characterize the behavior, we monitored the capacitance changes of the pressure sensor during compression testing (Figure S5, Supporting Information). The pressure sensor shows a wide detectable range in pressure (0-70 kPa), and the normalized capacitance (C/C_0) reaches 2.504 at the pressure of 70 kPa (Figure 6a). Due to the compliance of LMFCs, the pressure sensor can conform to curvilinear surfaces of human skin. We attached the pressure sensor onto the fingertip as a tactile sensor. The sensor can effectively detect the tapping motion of the fingertip against a table (Figure 6b). As an example, we generated Morse code from the pressure senor by tapping (Figure 6c).

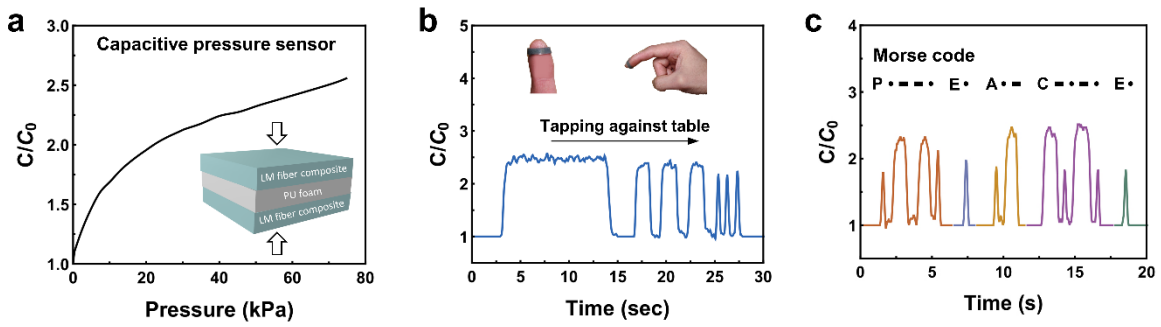

Figure 6. A capacitive pressure sensor consists of two LMFC soft electrodes and a PU foam core. a) Normalized capacitance of the sensor under uniform pressure. b) Response of the sensor under different tapping speed for tactile sensing usage on fingertips. c) The tactile sensor can generate Morse code 'PEACE' by tapping on the table surface.

5. Conclusions

In this work, we have introduced LMFC as a new paradigm of LM composites by embedding a LM fiber network into a silicone rubber matrix. Compared to existing LM particulate composites and co-continuous composites, LMFCs exhibit multiple advantages such as lightweight, superb stretchability, high conductivity, and cyclic stability. The LM fiber network is composed of LM-SEBS core-sheath microfibers with diameters in the range of 10-20 μm. The LM microfibers are fabricated by coaxial emulsion electrospinning to overcome a few technical challenges such as the high surface tension of LM and low strength of LM emulsion. This technique is able to fabricate LM fibers around 10 μm or even thinner, which fills a technology gap to fabricate LM fibers thinner than 100 μm. Upon mechanical sintering, the LMFC achieved an electric conductivity of 1.11 S/mm with merely 3.82 vol% of LM. Compared to other conductive LM composites, the LM volume fraction of our LMFCs is significantly lower (~10-fold reduction), which indicates that it is much cheaper and lighter. Under stretching, the resistance of LMFC remains almost constant when stretched to 400% strain. This remarkable feature of LMFCs is similar to the electromechanical behavior of LM particulate composites. Besides, the LMFCs exhibit outstanding stretchability (800% strain) and superior electrical stability under cyclic stretching.

Due to the prominent features, the developed LMFCs have high potential usage in stretchable circuits, soft electrodes, soft actuators, and biosensor. We successfully demonstrated that LMFCs can be utilized as interconnects in stretchable circuits. The circuits can maintain their functionality and integrity under various deformation modes like stretching, bending, and twisting. Additionally, we incorporated LMFCs as electrodes into capacitive strain sensors and

capacitive pressure sensors. The strain sensor can effectively detect the bending angle of fingers and the surface strain of a pneumatic actuator used in soft robotics. Future research can be towards filling the voids in the conductivity Ashby chart at the low-density regime. The conductivity of LMFCs can be further enhanced by optimizing the composition of core-sheath LM fibers, incorporating highly conductive hybrid fillers,[56] enhancing connectivity at fiber junctions, and developing better sintering methods. The concept we proposed in this work will broaden the applications of conductive LM composites.

6. Experimental Section

Solution Preparation: For the sheath solution, pellets of SEBS (styrene-ethylene-butylene-styrene; Kraton G-1657) were dissolved in a binary solvent of chloroform (Macron Fine Chemical) and toluene (Honeywell). The weight percentage of SEBS in the sheath solution was 16 wt%. The ratio of chloroform to toluene is 55:45 by weight. For the core solution, 4g of EGaIn (Ga 75.5 wt%, In 24.5 wt%) was added into a mixture of chloroform and 1-Dodecanethiol (1 mM/g, Sigma Aldrich). EGaIn microdroplets were produced using an ultrasonic probe (Branson 450 Sonifier). The amplitude and time of ultrasonication were 40% and 30 min, respectively. Then, the EGaIn microdroplets were mixed with SEBS, chloroform, and toluene to obtain a viscous liquid metal emulsion (EGaIn : SEBS = 4:1 by volume). The ratio of SEBS, chloroform, and toluene was 9:72.8:18.2 by weight. Both the core and sheath solutions were homogenized by a vortex mixer (VWR) for 15 h before the electrospinning process.

Coaxial Electrospinning: The as-prepared core and sheath solutions were transferred to 3 mL syringes, respectively. The coaxial electrospinning system consisted of two syringe pumps (NE-300, New Era Pump System Inc.), a 17/22 gauge coaxial needle (VECK, China), a DC high-voltage power supply (P030HP1, Acopian, USA) and a flat aluminum plate as a collector. The electrospinning process was performed in a fume hood. Flow rates of the core and sheath solution were set as 2 ml/h. The applied voltage was 10 kV and tip-to-collector distance was fixed as 16 cm. The obtained core-sheath microfiber mats were air-dried for 12 h in a fume hood.

Composite Fabrication: Ecoflex 00-30 (platinum-catalyzed silicone; Smooth-On Inc.) was infiltrated into the microfiber mat under vacuum in a mold. After curing at room temperature for 24 h, a LMFC film was obtained.

Mechanical Tensile Testing: Rectangular specimens (20mm × 3mm × 0.3mm) were tested on a tensile tester (eXpert 4000, ADMET Inc.) with a 5 N load cell. The initial gauge

length was 10mm and the extension rate was 10mm/min. Three specimens were tested for each type of sample.

Electromechanical Measurements: The microfiber mat was cut into desired sample sizes. Then, two ends of the fiber mat were pre-sintered (Figure S6, Supporting Information) and bonded to copper wires (leads) using conductive silver paste (843WB, MG Chemicals). After silicone impregnation and curing, the obtained composite film was sintered mechanically to activate electrical conductivity. Resistance of the composite was measured by a Keithley 2000 multimeter using four-wire measurement. Thickness of the composite was measured using an optical microscope, and electrical conductivity of the composite was calculated as $\sigma = l/wtR$, where l, w, t, and R are the length, width, thickness, and electrical resistance of the composite, respectively. The sintered composite specimens were tested on the tensile tester under monotonic or cyclic loading with the resistance measured by the multimeter meanwhile. The extension rate was 1% strain per second. For cyclic testing, a triangular strain profile was used with a frequency of 2 cycles/min for 100% strain and 1 cycle/min for 200% strain.

Demonstration as Interconnects: To fabricate stretchable circuits integrated with LED, the microfiber mat was cut into desired shapes, e.g., strips (3mm in width) or S-shapes. Areas on the mat strip that would connect to LEDs were pre-sintered. Then, pre-sintered area and LED were bonded together using the conductive silver paste. The integrated structures were encapsulated into Ecoflex 00-30 to obtain a stretchable circuit. After mechanical sintering, LEDs in the circuit can be lit up with a power supply.

Capacitive Strain Sensor: To fabricate capacitive strain sensors, sintered LMFCs (top and bottom layers) and Ecoflex 00-30 (middle layer) were bonded together with the aid of plasma treatment. The thickness of each layer was ~0.4mm. The strain-dependent capacitance of the sensor was characterized on the tensile tester with the capacitance measured by a Keithley 2110 multimeter simultaneously. The strain rate was controlled as 1.5% per second. Note that two ends of the sensor were bonded to acrylic plates so that the grip of the tensile tester won't compress the sensor directly.

Capacitive Pressure Sensor: A thin piece of polyurethane foam (500 μm thick) for pressure sensing is sliced from a bulk packaging foam using a slicer (SliceMaster, Jasco Inc.). The stress-strain relationship of the thin polyurethane foam under compression is shown in Figure S7. Sintered LMFCs (top and bottom layers) and the thin polyurethane foam (middle layer) were bonded together using silicone adhesive as a capacitive pressure sensor.

Capacitance change of the sensor was recorded while applying compressive strain by the ADMET tensile tester. The size of compression platens was 6mm × 6mm.

Supporting Information

Supporting Information is available from the Wiley Online Library or from the author.

Acknowledgements

This work is supported by National Science Foundation through the award CMMI-2143297. We also thank the support from the Small Scale Systems Integration and Packaging (S3IP) Center of Excellence, funded by New York Empire State Development's Division of Science, Technology and Innovation.

Received: ((will be filled in by the editorial staff))

Revised: ((will be filled in by the editorial staff))

Published online: ((will be filled in by the editorial staff))

References

[1] H. Joo, D. Jung, S.-H. Sunwoo, J. H. Koo, D.-H. Kim, *Small* **2020**, *16*, 1906270.
[2] S. Wang, Y. Nie, H. Zhu, Y. Xu, S. Cao, J. Zhang, Y. Li, J. Wang, X. Ning, D. Kong, *Sci. Adv.* **2022**, *8*, eabl5511.
[3] X. Su, X. Wu, S. Chen, A. M. Nedumaran, M. Stephen, K. Hou, B. Czarny, W. L. Leong, *Advanced Materials* **2022**, *34*, 2200682.
[4] L. Xu, Z. Huang, Z. Deng, Z. Du, T. L. Sun, Z. Guo, K. Yue, *Advanced Materials* **2021**, *33*, 2105306.
[5] M. D. Dickey, *Adv. Mater.* **2017**, *29*, 1606425.
[6] E. Palleau, S. Reece, S. C. Desai, M. E. Smith, M. D. Dickey, *Adv. Mater.* **2013**, *25*, 1589.
[7] S. Choi, S. I. Han, D. Kim, T. Hyeon, D.-H. Kim, *Chem. Soc. Rev.* **2019**, *48*, 1566.
[8] G. Yun, S.-Y. Tang, H. Lu, S. Zhang, M. D. Dickey, W. Li, *Small Science* **2021**, *1*, 2000080.
[9] R. W. Style, R. Tutika, J. Y. Kim, M. D. Bartlett, *Adv. Funct. Mater.* **2021**, *31*, 2005804.
[10] Q. Gui, Y. He, Y. Wang, *Adv. Electron. Mater.* **2021**, *7*, 2000780.
[11] E. J. Markvicka, M. D. Bartlett, X. Huang, C. Majidi, *Nat. Mater.* **2018**, *17*, 618.
[12] L. Mou, J. Qi, L. Tang, R. Dong, Y. Xia, Y. Gao, X. Jiang, *Small* **2020**, *16*, 2005336.
[13] H. Wang, Y. Yao, Z. He, W. Rao, L. Hu, S. Chen, J. Lin, J. Gao, P. Zhang, X. Sun, X. Wang, Y. Cui, Q. Wang, S. Dong, G. Chen, J. Liu, *Adv. Mater.* **2019**, *31*, 1901337.
[14] M. J. Ford, C. P. Ambulo, T. A. Kent, E. J. Markvicka, C. Pan, J. Malen, T. H. Ware, C. Majidi, *Proc. Natl. Acad. Sci. U.S.A.* **2019**, *116*, 21438.
[15] M. J. Ford, D. K. Patel, C. Pan, S. Bergbreiter, C. Majidi, *Advanced Materials* **2020**, *32*, 2002929.
[16] A. Fassler, C. Majidi, *Adv. Mater.* **2015**, *27*, 1928.
[17] R. Tutika, A. B. M. T. Haque, M. D. Bartlett, *Commun Mater* **2021**, *2*, 64.
[18] Y. Xin, H. Peng, J. Xu, J. Zhang, *Adv. Funct. Mater.* **2019**, *29*, 1808989.

[19] M. G. Saborio, S. Cai, J. Tang, M. B. Ghasemian, M. Mayyas, J. Han, M. J. Christoe, S. Peng, P. Koshy, D. Esrafilzadeh, R. Jalili, C. H. Wang, K. Kalantar-Zadeh, *Small* **2020**, *16*, 1903753.
[20] A. M. Nasab, S. Sharifi, S. Chen, Y. Jiao, W. Shan, *Adv. Intell. Syst.* **2021**, *3*, 2000166.
[21] X. Pan, D. Guo, H. He, *J. Phys. D: Appl. Phys.* **2021**, *54*, 085401.
[22] D. Yu, Y. Liao, Y. Song, S. Wang, H. Wan, Y. Zeng, T. Yin, W. Yang, Z. He, *Adv. Sci.* **2020**, *7*, 2000177.
[23] B. Yao, W. Hong, T. Chen, Z. Han, X. Xu, R. Hu, J. Hao, C. Li, H. Li, S. E. Perini, M. T. Lanagan, S. Zhang, Q. Wang, H. Wang, *Advanced Materials* **2020**, *32*, 1907499.
[24] S. Liang, Y. Li, Y. Chen, J. Yang, T. Zhu, D. Zhu, C. He, Y. Liu, S. Handschuh-Wang, X. Zhou, *J. Mater. Chem. C* **2017**, *5*, 1586.
[25] N. Ning, W. Huang, S. Liu, Q. Zhao, H. Zou, B. Yu, M. Tian, L. Zhang, *Composites Part B: Engineering* **2019**, *179*, 107492.
[26] X. Xue, D. Zhang, Y. Wu, R. Xing, H. Li, T. Yu, B. Bai, Y. Tao, M. D. Dickey, J. Yang, *Adv Funct Materials* **2023**, *33*, 2210553.
[27] E. J. Krings, H. Zhang, S. Sarin, J. E. Shield, S. Ryu, E. J. Markvicka, *Small* **2021**, *17*, 2104762.
[28] W. Lee, H. Kim, I. Kang, H. Park, J. Jung, H. Lee, H. Park, J. S. Park, J. M. Yuk, S. Ryu, J.-W. Jeong, J. Kang, *Science* **2022**, *378*, 637.
[29] H. Wang, R. Li, Y. Cao, S. Chen, B. Yuan, X. Zhu, J. Cheng, M. Duan, J. Liu, *Adv. Fiber Mater.* **2022**.
[30] S. He, C. Zhou, H. Chen, X. Liu, H. Li, W. Ma, X. Su, T. Han, *J. Mater. Chem. C* **2020**, *8*, 3553.
[31] Q. Zhuang, Z. Ma, Y. Gao, Y. Zhang, S. Wang, X. Lu, H. Hu, C. Cheung, Q. Huang, Z. Zheng, *Advanced Functional Materials* **2021**, *31*, 2105587.
[32] N. Zhou, B. Jiang, X. He, Y. Li, Z. Ma, H. Zhang, M. Zhang, *ACS Appl. Mater. Interfaces* **2021**, *13*, 19254.
[33] X. Ma, M. Zhang, J. Zhang, S. Wang, S. Cao, Y. Li, G. Hu, D. Kong, *ACS Materials Lett.* **2022**, *4*, 634.
[34] Z. Ma, Q. Huang, Q. Xu, Q. Zhuang, X. Zhao, Y. Yang, H. Qiu, Z. Yang, C. Wang, Y. Chai, Z. Zheng, *Nat. Mater.* **2021**, *20*, 859.
[35] S. Zhu, J.-H. So, R. Mays, S. Desai, W. R. Barnes, B. Pourdeyhimi, M. D. Dickey, *Advanced Functional Materials* **2013**, *23*, 2308.
[36] Y. Wu, R. Zhen, H. Liu, S. Liu, Z. Deng, P. Wang, S. Chen, L. Liu, *J. Mater. Chem. C* **2017**, *5*, 12483.
[37] Y. Yu, J. Guo, B. Ma, D. Zhang, Y. Zhao, *Science Bulletin* **2020**, *65*, 1752.
[38] A. Leber, C. Dong, R. Chandran, T. Das Gupta, N. Bartolomei, F. Sorin, *Nat Electron* **2020**, *3*, 316.
[39] X. Yu, W. Fan, Y. Liu, K. Dong, S. Wang, W. Chen, Y. Zhang, L. Lu, H. Liu, Y. Zhang, *Advanced Materials Technologies* **2022**, *n/a*, 2101618.
[40] L. Zheng, M. Zhu, B. Wu, Z. Li, S. Sun, P. Wu, *Sci. Adv.* **2021**, *7*, eabg4041.
[41] C. Dong, A. Leber, T. Das Gupta, R. Chandran, M. Volpi, Y. Qu, T. Nguyen-Dang, N. Bartolomei, W. Yan, F. Sorin, *Nat Commun* **2020**, *11*, 3537.
[42] M. Song, K. Kartawira, K. D. Hillaire, C. Li, C. B. Eaker, A. Kiani, K. E. Daniels, M. D. Dickey, *Proceedings of the National Academy of Sciences* **2020**, *117*, 19026.
[43] L.-C. Jia, X.-X. Jia, W.-J. Sun, Y.-P. Zhang, L. Xu, D.-X. Yan, H.-J. Su, Z.-M. Li, *ACS Appl. Mater. Interfaces* **2020**, *12*, 53230.
[44] J. Han, J. Tang, S. A. Idrus-Saidi, M. J. Christoe, A. P. O'Mullane, K. Kalantar-Zadeh, *ACS Appl. Mater. Interfaces* **2020**, *12*, 31010.
[45] L. Long, X. Che, P. Yao, X. Zhang, J. Wang, M. Li, C. Li, *ACS Appl. Mater. Interfaces* **2022**, *14*, 18690.

[46] M. R. Khan, C. B. Eaker, E. F. Bowden, M. D. Dickey, *Proc. Natl. Acad. Sci. U.S.A.* **2014**, *111*, 14047.
[47] J. N. Koster, *Cryst. Res. Technol.* **1999**, *34*, 1129.
[48] Q. Ye, Y. Wu, Y. Qi, L. Shi, S. Huang, L. Zhang, M. Li, W. Li, X. Zeng, H. Wo, X. Wang, S. Dong, S. Ramakrishna, J. Luo, *Nano Energy* **2019**, *61*, 381.
[49] Z. Sha, C. Boyer, G. Li, Y. Yu, F.-M. Allioux, K. Kalantar-Zadeh, C.-H. Wang, J. Zhang, *Nano Energy* **2022**, *92*, 106713.
[50] J. Zhu, Y. Wu, X. Huang, L. Huang, M. Cao, G. Song, X. Guo, X. Sui, R. Ren, J. Chen, *Nano Energy* **2019**, *62*, 883.
[51] M. H. Malakooti, M. R. Bockstaller, K. Matyjaszewski, C. Majidi, *Nanoscale Adv.* **2020**, *2*, 2668.
[52] J. W. Boley, E. L. White, R. K. Kramer, *Adv. Mater.* **2015**, *27*, 2355.
[53] Y. Liu, X. Ji, J. Liang, *npj Flex Electron* **2021**, *5*, 11.
[54] N. Zolfaghari, P. Khandagale, M. J. Ford, K. Dayal, C. Majidi, *Soft Matter* **2020**, *16*, 8818.
[55] Y. Zhao, P. Khandagale, C. Majidi, *Extreme Mechanics Letters* **2021**, *48*, 101443.
[56] K. Parida, G. Thangavel, G. Cai, X. Zhou, S. Park, J. Xiong, P. S. Lee, *Nat Commun* **2019**, *10*, 2158.

Table of contents

Liquid metal fiber composites are introduced as a new paradigm of conductive liquid metal composites. This composite exhibits low density, superb stretchability, high conductivity, and cyclic stability. High conductivity is achieved with less than 4 vol% of liquid metal.

J. Ma, Z. Liu, Q. Nguyen, P. Zhang*

Lightweight Soft Conductive Composites Embedded with Liquid Metal Fiber Networks

ToC figure (size: 55 mm broad × 50 mm)

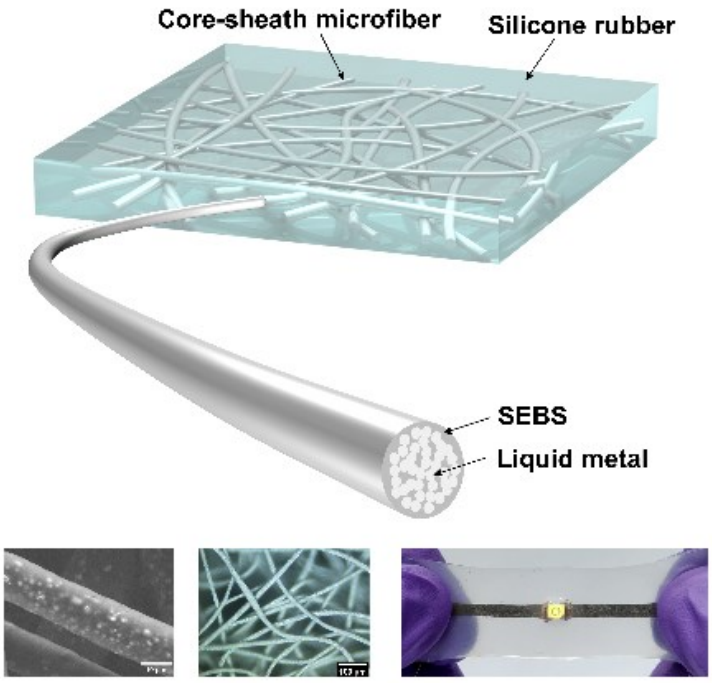

Supporting Information

Lightweight Soft Conductive Composites Embedded with Liquid Metal Fiber Networks

*Jiexian Ma, Zihan Liu, Quang-Kha Nguyen, and Pu Zhang**

Table S1. Electrical conductivity of LM composites in the literature.

Ref.	Material	CompositeType	Volume Fraction of Liquid Metal [%]	Electrical Conductivity [S/mm]
[1]	Galinstan / PDMS	Co-continuous	75	1620
[2]	BiInSn / PDMS	Co-continuous	25	180
[3]	Galinstan / PU	Co-continuous	65	1890
			90	2670
[4]	EGaIn / PDMS	Co-continuous	30	530
[5]	GaInZn / Sulfur polymer	Particulate	30	0.43
			50	1.8
[6]	EGaIn / Liquid crystal elastomers	Particulate	50	20
[7]	Galinstan / PDMS	Particulate	50	10.5
[8]	EGaIn / PDMS	Particulate	50	137
[9]	EGaIn / PDMS	Particulate	50	1
			70	17
[10]	EGaIn / PDMS	Particulate	40	56.18
[11]	EGaIn / SIS polymer	Particulate	60	15
[12]	EGaIn / SBS polymer	Particulate	40	8
			60	560
			80	1200

Table S1. (continuned)

Ref.	Material	Type	Volume Fraction of Liquid Metal [%]	Electrical Conductivity [S/mm]
[13]	EGaIn / TPU	Particulate	49.2	74.5
			57.5	427
			63.5	698
			68	1051
			71.6	1552
			74.4	2100
[14]	Galinstan / PDMS / PDMS particles	Particulate	60	0.438
			60	2.17
			55	0.042435
			46	0.04182
			40	0.00668

References

[1] S. Liang, Y. Li, Y. Chen, J. Yang, T. Zhu, D. Zhu, C. He, Y. Liu, S. Handschuh-Wang, X. Zhou, *J. Mater. Chem. C* **2017**, *5*, 1586.

[2] D. Yu, Y. Liao, Y. Song, S. Wang, H. Wan, Y. Zeng, T. Yin, W. Yang, Z. He, *Adv. Sci.* **2020**, *7*, 2000177.

[3] N. Ning, W. Huang, S. Liu, Q. Zhao, H. Zou, B. Yu, M. Tian, L. Zhang, *Composites Part B: Engineering* **2019**, *179*, 107492.

[4] B. Yao, W. Hong, T. Chen, Z. Han, X. Xu, R. Hu, J. Hao, C. Li, H. Li, S. E. Perini, M. T. Lanagan, S. Zhang, Q. Wang, H. Wang, *Advanced Materials* **2020**, *32*, 1907499.

[5] Y. Xin, H. Peng, J. Xu, J. Zhang, *Adv. Funct. Mater.* **2019**, *29*, 1808989.

[6] M. J. Ford, C. P. Ambulo, T. A. Kent, E. J. Markvicka, C. Pan, J. Malen, T. H. Ware, C. Majidi, *Proc. Natl. Acad. Sci. U.S.A.* **2019**, *116*, 21438.

[7] A. Fassler, C. Majidi, *Adv. Mater.* **2015**, *27*, 1928.

[8] E. J. Markvicka, M. D. Bartlett, X. Huang, C. Majidi, *Nat. Mater.* **2018**, *17*, 618.

[9] M. J. Ford, D. K. Patel, C. Pan, S. Bergbreiter, C. Majidi, *Advanced Materials* **2020**, *32*, 2002929.

[10] H. Wang, Y. Yao, Z. He, W. Rao, L. Hu, S. Chen, J. Lin, J. Gao, P. Zhang, X. Sun, X. Wang, Y. Cui, Q. Wang, S. Dong, G. Chen, J. Liu, *Adv. Mater.* **2019**, *31*, 1901337.

[11] R. Tutika, A. B. M. T. Haque, M. D. Bartlett, *Commun Mater* **2021**, *2*, 64.

[12] L. Mou, J. Qi, L. Tang, R. Dong, Y. Xia, Y. Gao, X. Jiang, *Small* **2020**, *16*, 2005336.

[13] W. Lee, H. Kim, I. Kang, H. Park, J. Jung, H. Lee, H. Park, J. S. Park, J. M. Yuk, S. Ryu, J.-W. Jeong, J. Kang, *Science* **2022**, *378*, 637.

[14] X. Xue, D. Zhang, Y. Wu, R. Xing, H. Li, T. Yu, B. Bai, Y. Tao, M. D. Dickey, J. Yang, *Adv Funct Materials* **2023**, *33*, 2210553.

Table S2. Comparison between this work and previous study concerning electrospun LM fibers. The major difference is stretchability and conductivity.

Ref.	Materials	Fiber diameter	Volume fraction of LM within fiber [%]	Applications	Note
15	LM particles + PAN	Nanofibers	0.35	TENG	Non-stretchable Non-conductive
16	LM particles + PVDF-HFP	Nanofibers	0.56	TENG	Non-stretchable Non-conductive
17	LM particles + SAN + PAN	1-2 µm	6.5	Lithium-ion batteries	Non-stretchable Conductive after carbonization (600 °C) Low conductivity
This work	LM particles + SEBS	8 - 40 µm	50-60 (overall) 80 (core)	Stretchable conductor	Highly stretchable. Highly conductive after mechanical sintering

References

[15] Q. Ye, Y. Wu, Y. Qi, L. Shi, S. Huang, L. Zhang, M. Li, W. Li, X. Zeng, H. Wo, X. Wang, S. Dong, S. Ramakrishna, J. Luo, Nano Energy 2019, 61, 381.

[16] Z. Sha, C. Boyer, G. Li, Y. Yu, F.-M. Allioux, K. Kalantar-Zadeh, C.-H. Wang, J. Zhang, Nano Energy 2022, 92, 106713.

[17] J. Zhu, Y. Wu, X. Huang, L. Huang, M. Cao, G. Song, X. Guo, X. Sui, R. Ren, J. Chen, Nano Energy 2019, 62, 883.

Table S3. Electrical conductivity of LMFC composites fabricated in the paper.

Type of composite	Volume Fraction of EGaIn [a] [%]	Electrical Conductivity [S/mm]	Note
LMFC (recipe 1)	3.82	1.11	Random fiber network
LMFC (recipe 1)	3.82	0.74	Random fiber network
LMFC (recipe 2)	2.46	0.563	Random fiber network
LMFC (recipe 2)	6.4	1.37	Random fiber network
LMFC (recipe 3)	5.1	0.147	Random fiber network
LMFC (recipe 3)	4.7	0.204	Random fiber network
Aligned LM fiber composite [b]	3.8	0.604	Aligned fiber
Aligned LM fiber composite	9.4	1.22	Aligned fiber

[a]The volume fraction of EGaIn in the composite is calculated according to the composition of electrospinning solution and the weight percentage of fiber mat in the composite.

[b]Aligned LM fibers were collected by a drum collector.

Table S4. Influence of temperature on the performance of mechanical sintering. LMFC is heated on a hot plate, and then sintered by mechanical stress.

Temperature [°C]	Resistance [Ω]
25	15.6
130	12.1
150	10.3
180	10.3

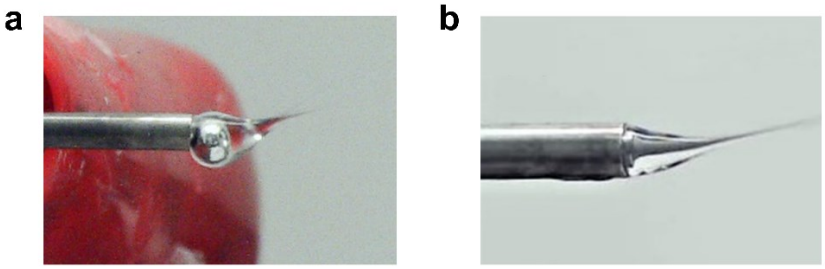

Figure S1. a) Coaxial electrospinning with a LM core and a SEBS sheath fluid. A spherical LM bubble was formed in the Taylor cone due to the high surface tension of LM. b) Coaxial emulsion electrospinning with a LM-SEBS emulsion as the core fluid and a SEBS solution as sheath fluid. A stable compound Taylor cone was formed at the nozzle tip.

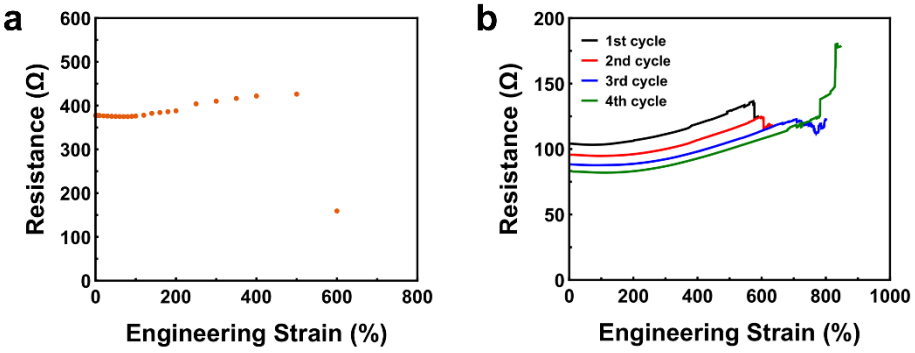

Figure S2. Mechanical sintering of LMFCs by stretching: a) monotonic loading. b) multiple stretching cycles.

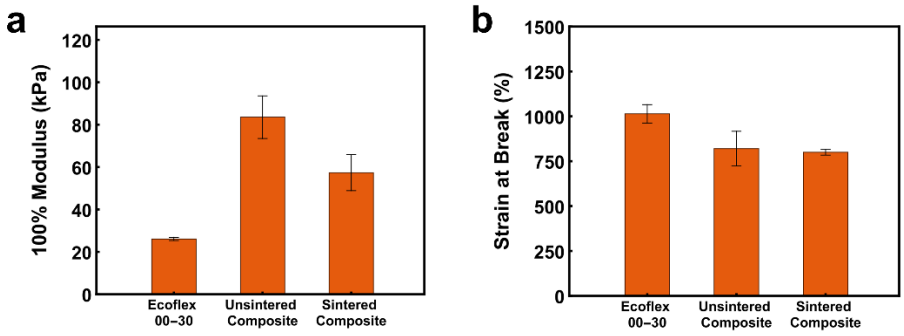

Figure S3. a) 100% modulus (stress at 100% strain) and b) strain at break for Ecoflex 00-30, LMFC without sintering, and sintered LMFC under uniaxial tensile testing.

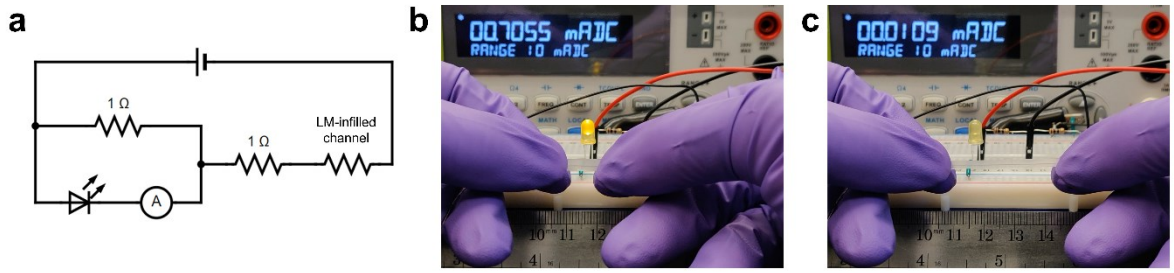

Figure S4. Interconnects with a LM-infilled channel. a) An LED circuit with LM channel as connected wire: b) before stretching (initial gauge length: 1 cm, 0.7055mA), and c) after stretching (gauge length: 3.5 cm, ~250% strain, 0.0109mA). The brightness of the LED darken drastically due to the significant resistance change of the LM channel under stretching. This resistance follows the Pouillet's law.

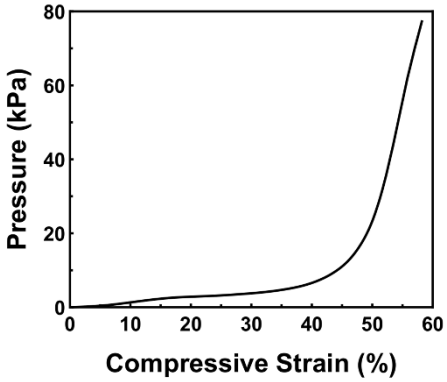

Figure S5. Pressure versus compressive strain when the capacitive pressure sensor shown in the paper is under compression testing.

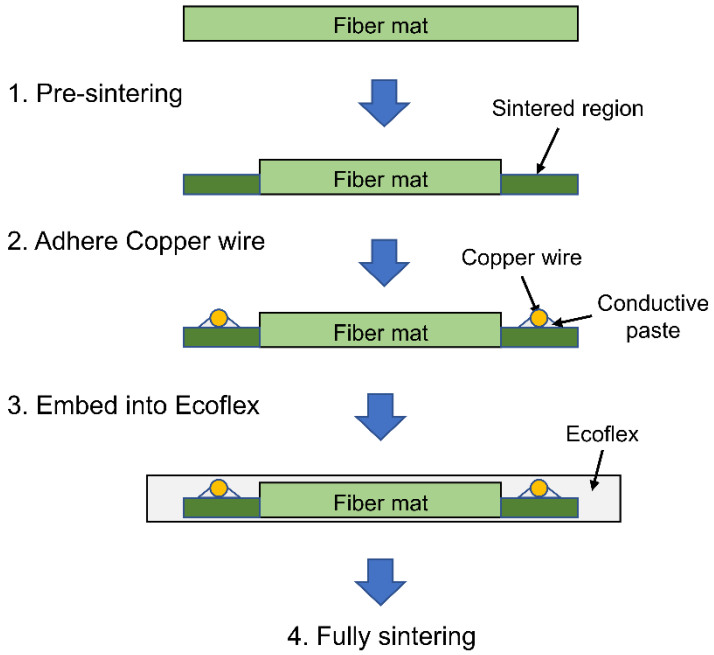

Figure S6. The preparation procedure of LMFC for resistance measurement.

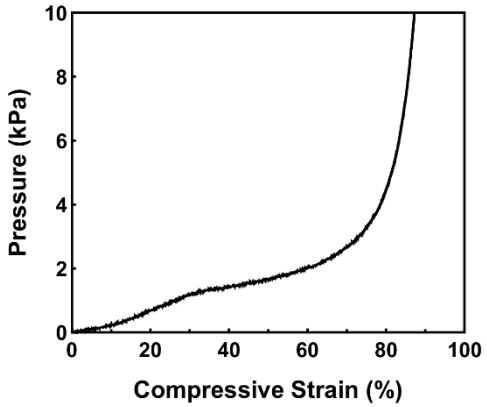

Figure S7. Pressure versus compressive strain when the polyurethane foam is under compression testing.